



## Degradation of $\text{LaSr}_2\text{Fe}_2\text{CrO}_{9-\delta}$ solid oxide fuel cell anodes in phosphine-containing fuels

Mingyang Gong<sup>a</sup>, David Bierschenk<sup>b</sup>, J. Haag<sup>c</sup>, K.R. Poeppelmeier<sup>c</sup>, Scott A. Barnett<sup>b</sup>, Chunchuan Xu<sup>d</sup>, John W. Zondlo<sup>d</sup>, Xingbo Liu<sup>a,\*</sup>

<sup>a</sup> Department of Mechanical and Aerospace Engineering, West Virginia University, Morgantown, WV 26506, USA

<sup>b</sup> Department of Materials Science and Engineering, Northwestern University, Evanston, IL 60208, USA

<sup>c</sup> Department of Chemistry, Northwestern University, Evanston, IL 60208, USA

<sup>d</sup> Department of Chemical Engineering, West Virginia University, Morgantown, WV 26506, USA

### ARTICLE INFO

#### Article history:

Received 16 December 2009

Received in revised form

22 December 2009

Accepted 22 December 2009

Available online 13 January 2010

#### Keywords:

SOFC

$\text{LaSr}_2\text{Fe}_2\text{CrO}_{9-\delta}$  anode

Hydrogen

Coal syngas

Phosphine

### ABSTRACT

The performance and stability of  $\text{La}_{0.9}\text{Sr}_{0.1}\text{Ga}_{0.8}\text{Mg}_{0.2}\text{O}_{3-\delta}$ -electrolyte supported solid oxide fuel cells with composite  $\text{LaSr}_2\text{Fe}_2\text{CrO}_{9-\delta}$ - $\text{Gd}_{0.1}\text{Ce}_{0.9}\text{O}_2$  anodes were studied in wet  $\text{H}_2$  and coal syngas containing phosphine impurity. Introduction of 5–20 ppm  $\text{PH}_3$  into the fuels caused an initial slow cell performance degradation followed by a very rapid complete cell degradation that initiated within 11–24 h – earlier at higher  $\text{PH}_3$  concentration. There was no recovery after removing  $\text{PH}_3$  impurity from the fuels. Electrochemical impedance analysis suggested that the initial gradual performance degradation was due to conductivity loss of the oxide anode due to chemisorption and reaction of phosphine. X-ray diffraction analysis showed the formation of  $\text{FeP}_x$  and  $\text{LaPO}_4$  compounds. The rapid degradation presumably occurred when most or all of the Fe initially present in the  $\text{LaSr}_2\text{Fe}_2\text{CrO}_{9-\delta}$  was consumed. Thermodynamic calculations confirmed that Fe is highly reactive with  $\text{PH}_3$  at 800 °C, even at concentrations below 1 ppm.

© 2010 Elsevier B.V. All rights reserved.

### 1. Introduction

There is a widespread reliance on coal in the electrical power industry. However, cleaner and more  $\text{CO}_2$ -neutral methods of utilizing coal are required in order to make use of abundant worldwide coal reserves. Solid oxide fuel cells (SOFCs) are being actively developed for clean and fuel-efficient stationary electrical power generation; they are of particular interest for coal-based generation [1,2] since they oxidize coal-derived syngas with pure oxygen, producing a  $\text{CO}_2$ -rich product that allows for easier and lower cost sequestration compared to  $\text{N}_2$ -rich air-combustion products. An additional advantage of SOFCs is their ability to utilize fuels containing various species in addition to hydrogen, such as CO, hydrocarbons, and impurities. Thus, SOFC-based power plants can be designed with reduced fuel processing and clean-up requirements compared to other fuel cells, reducing power plant cost.

Coals contain a large number of different impurities. A recent study examined the coal impurities expected to be present in

the syngas after gasification with warm-gas clean-up and found  $\text{H}_2\text{S}$ ,  $\text{PH}_3$ , and  $\text{AsH}_3$  to be the most problematic due to their reactivity with typical Ni-based SOFC anodes [3]. Degradation of Ni-cermet anode performance has been shown to occur at ppm levels of  $\text{H}_2\text{S}$ , and more serious damage at higher levels. Recent studies have shown that Ni-YSZ anodes are rapidly attacked by  $\text{AsH}_3$  and  $\text{PH}_3$  at few ppm levels, resulting in the formation of  $\text{NiAs}_x$  and  $\text{NiP}_x$  compounds [4,5]. More extensive syngas clean-up is possible, but not without additional system costs and loss in system efficiency [3,6]. Thus, alternative anode materials with improved tolerance to fuel impurities are of interest. Perovskite oxides, some of which are mixed ionic and electronic conductors (MIEC), have been shown to have superior resistance to carbon deposition and sulfur poisoning when compared to Ni-cermet [7–10]. Several perovskite and perovskite-related anodes, such as  $\text{La}_{0.75}\text{Sr}_{0.25}\text{Cr}_{0.5}\text{Fe}_{0.5}\text{O}_3$  [11],  $\text{La}_{0.75}\text{Sr}_{0.25}\text{Cr}_{0.5}\text{Mn}_{0.5}\text{O}_3$  (LSCM) [12],  $\text{Sr}_2\text{Mg}_{1-x}\text{Mn}_x\text{MoO}_{6-\delta}$  [13], and  $\text{LaSr}_2\text{Fe}_2\text{CrO}_{9-\delta}$  (LSFeCr) mixed with  $\text{Gd}_{0.1}\text{Ce}_{0.9}\text{O}_2$  (GDC) [14] have been demonstrated with hydrogen and/or methane fuels, exhibiting electrochemical performance that was good but usually inferior to that of nickel cermet. In some cases, good tolerance to  $\text{H}_2\text{S}$  impurities has been demonstrated [15]. However, little is known about the performance and stability of oxide anodes in the presence of ppm levels of  $\text{PH}_3$ , and  $\text{AsH}_3$ .

\* Corresponding author at: Department of Mechanical and Aerospace Engineering, West Virginia University, P.O. Box 6106, Morgantown, WV 26506, USA. Tel.: +1 304 293 3339; fax: +1 304 293 6689.

E-mail address: [xingbo.liu@mail.wvu.edu](mailto:xingbo.liu@mail.wvu.edu) (X. Liu).

In the present report, SOFCs with LSCr–GDC composite anodes were evaluated for operation in simulated coal syngas containing 5–20 ppm  $\text{PH}_3$ , and humidified  $\text{H}_2$  for comparison. SOFC performance degradation and anode phase transitions caused by  $\text{PH}_3$ -poisoning were investigated.

## 2. Experimental

### 2.1. Cell description

The SOFCs consisted of  $\text{La}_{0.9}\text{Sr}_{0.1}\text{Ga}_{0.8}\text{Mg}_{0.2}\text{O}_{3-\delta}$  (LSGM) electrolyte supports with  $\approx 10\text{-}\mu\text{m}$ -thick  $\text{La}_{0.4}\text{Ce}_{0.6}\text{O}_2$  (LDC) layers on the anode side, LSCr–GDC composite anode,  $\text{La}_{0.6}\text{Sr}_{0.4}\text{Fe}_{0.8}\text{Co}_{0.2}\text{O}_{3-\delta}$  (LSCF)–GDC cathode, and LSCF cathode current collector. The LDC layer was used to prevent any reaction/interdiffusion between the LSGM and LSCr during anode firing. The fabrication and performance of these cells was similar to that described previously [14].

The LSGM was prepared via solid-state reaction. Appropriate quantities of  $\text{La}_2\text{O}_3$ ,  $\text{SrCO}_3$ ,  $\text{Ga}_2\text{O}_3$ , and  $\text{MgO}$  were mixed and calcined at  $1250^\circ\text{C}$  for 12 h. The resulting powder was mixed with poly(vinyl butyral) (PVB), ground, and pressed into 19 mm diameter pellets weighing 0.45 g. The resulting pellets were bisque fired at  $1200^\circ\text{C}$  for 10 h. The LDC layer was then applied by drop-coating a colloidal solution of LDC to the bisque fired pellets. The resulting structures were sintered at  $1450^\circ\text{C}$  for 6 h.

LSCr was prepared by solid-state reaction. Stoichiometric quantities of  $\text{La}_2\text{O}_3$ ,  $\text{SrCO}_3$ ,  $\text{Cr}_2\text{O}_3$ , and  $\text{Fe}_2\text{O}_3$  were mixed and calcined at  $1200^\circ\text{C}$  for 6 h. The resulting powder was ball milled in ethanol with GDC (1:1 weight ratio) for 24 h. The resulting slurry was dried, sieved, and mixed with a vehicle (Heraeus V-737) using a three roll mill. The LSCF–GDC cathode ink was prepared by mixing commercial LSCF powder (Praxair) and GDC (1:1 weight ratio) and adding a vehicle, whereas the current collector ink was prepared with pure LSCF. The thick-film LSCr–GDC anodes were applied with the doctor blade technique and fired at  $1200^\circ\text{C}$  for 3 h. The cathodes and cathode current collectors were applied in a similar manner and fired at  $1000^\circ\text{C}$  for 3 h. Au current collector grids were applied to both electrodes by screen printing Au ink (Heraeus Inc., PA). The resulting fuel cells had a diameter of  $\sim 1.5$  cm, and electrode thicknesses of 20–30  $\mu\text{m}$ . The anode and cathode areas were both  $0.5\text{ cm}^2$  and defined the cell active area.

### 2.2. Fuel cell testing setup

A schematic of the cell test setup is presented in Fig. 1. Pt meshes were attached to both the anode and the cathode surface using Pt paste. Ag wires were then welded to the Pt meshes to provide current supply and voltage measurement leads respectively. The button cell assembly was mounted between two alumina flanges with compressive mica gasket as seals. This cell setup was then placed between two alumina tubes inside a vertical furnace. The anode-side tube confined the fuel and the cathode-side tube confined the air. The mica seal was softened/sealed in situ prior to cell operation at  $800^\circ\text{C}$ . The air flow was maintained at a constant level of 300 standard cubic centimeter per min (sccm). Humidified hydrogen (3%  $\text{H}_2\text{O}$ ) or surrogate coal syngas was applied as the fuel at 200 sccm. Fuel mixtures were controlled with mass flow controllers from Alicat Co. (AZ, USA). The surrogate syngas mixture was obtained by blending the wet  $\text{H}_2$  with CO and  $\text{CO}_2$ . The resulting coal syngas mixture contained 30%  $\text{H}_2$ , 26%  $\text{H}_2\text{O}$ , 23% CO, and 21%  $\text{CO}_2$ . Thermodynamic calculations (FACTSAGE v5.4) for this composition indicated that the water gas shift reaction ( $\text{CO} + \text{H}_2\text{O} \rightarrow \text{CO}_2 + \text{H}_2$ ) was at equilibrium at 1073 K. A similar calculation also predicted the present fuel composition, with

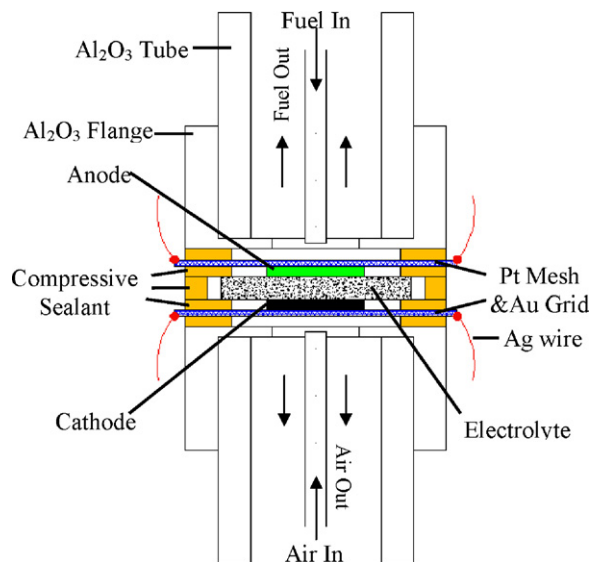


Fig. 1. Sketch of the cell testing setup.

a steam/carbon (S/C) ratio of 0.62, did not favor coke formation [8].

### 2.3. $\text{PH}_3$ testing procedure

The stability of LSCr–GDC in the presence of  $\text{PH}_3$  was studied as a function of fuel type and impurity concentration. Cells were tested in surrogate syngas and humidified hydrogen containing 0 ppm, 5 ppm, or 20 ppm of  $\text{PH}_3$ . It should be noted that coal syngas, after clean-up, typically contains  $\sim 1$  ppm  $\text{PH}_3$  [3]. The present phosphine concentrations are significantly higher and therefore the anode degradation should occur at an accelerated rate. The specific testing conditions for each sample are summarized in Table 1.

The LSCr–GDC cells were heated in air to  $800^\circ\text{C}$  and then supplied sequentially with 10% $\text{H}_2$ /90% $\text{N}_2$ , 50% $\text{H}_2$ /50% $\text{N}_2$ , and then dry  $\text{H}_2$ . Afterwards, the fuel was switched to 200 sccm humidified  $\text{H}_2$  or the surrogate coal syngas and was allowed to stabilize at an operating voltage of  $\sim 0.7$  V. The  $\text{PH}_3$  impurity was then introduced into the fuel flow and the cell performance and stability were monitored by measuring the cell voltage, AC impedance and current–voltage characteristics. Electrochemical measurements were carried out with an electrochemical interface SI-1287 and an SI-1260 impedance analyzer (Solartron Instruments, Hampshire, UK). Impedances of the cell at open circuit voltage (OCV) and under DC biases were taken at frequencies ranging from  $10^{-1}$  Hz to  $10^5$  Hz with an AC signal amplitude of 20 mV. The series resistance ( $R_s$ ) of the cells was obtained from the high-frequency intercept on the Nyquist diagrams. Cell polarization resistances ( $R_p$ ) were taken as the difference between the low frequency and the high-frequency real-axis intercepts of the impedance curves. After testing on  $\text{PH}_3$ -laden fuel, cells were tested again in dry  $\text{H}_2$ . Cells were cooled in  $\text{N}_2$  after testing.

Table 1  
Summary of testing conditions for CG-Fe cells.

Sample ID	Test conditions
CG-P0	$T = 800^\circ\text{C}$ , $j = 0.25\text{ A cm}^{-2}$ , coal syngas mixture
CG-P20	$T = 800^\circ\text{C}$ , $j = 0.25\text{ A cm}^{-2}$ , coal syngas mixture with 20 ppm $\text{PH}_3$ ; total exposure time in $\text{PH}_3 = 10$ h
H2-P20	$T = 800^\circ\text{C}$ , $j = 0.5\text{ A cm}^{-2}$ , 97% $\text{H}_2$ /3% $\text{H}_2\text{O}$ with 20 ppm $\text{PH}_3$ ; total exposure time in $\text{PH}_3 = 15$ h
H2-P5	$T = 800^\circ\text{C}$ , $j = 0.25\text{ A cm}^{-2}$ , 97% $\text{H}_2$ /3% $\text{H}_2\text{O}$ with 5 ppm $\text{PH}_3$ ; total exposure time in $\text{PH}_3 = 22$ h

## 2.4. Post-test characterization

Anode surfaces and cell cross-sections were examined using a Hitachi S-4700 scanning electron microscope (SEM). Energy dispersive X-ray spectrometry (EDS) was completed using the SEM system and was utilized to check for the presence of phosphorous in the anode. X-ray diffraction (XRD) was carried out to determine the phases present in the anode using an X-pert Pro 3040 PANalytical system (Cu  $K\alpha$  radiation at 45 kV). The XRD patterns of an as-processed cell, baseline anode after clean syngas exposure, and anodes tested with  $PH_3$ -laden fuels were obtained at scanning rates of  $0.005\text{--}0.03^\circ\text{ s}^{-1}$ . Phase identification was completed using the X'Pert Highscore Plus 2.0 software and the PDF2-2004 electronic database.

X-ray photoelectron spectroscopy (XPS) tests were performed using a PHI 5000 Versa Probe system in order to analyze the elemental electron state and chemical composition of the LSFerCr anode surface after  $PH_3$  exposure. A monochromatic Al  $K\alpha$  radiation source (1486.6 eV) at an operating power of 300 W was used. The Pt mesh was peeled off the anode surfaces prior to XPS measurement. Since there was a peak drift due to surface charging, all of the peaks were identified by shifting the C1s peak to 284.8 eV, which is the standard peak for hydrocarbon species [16]. Both survey scans and element-specific scans were completed. Peak identification was aided using the National Institute of Standard and Technology (NIST) XPS database.

To clarify the anode degradation mechanism from reaction with  $PH_3$ , a thermodynamic analysis was carried out using FACTSAGE 5.4. Possible phases that could form were calculated by minimizing the Gibbs free energy change for reactions involving the anode constituents and  $PH_3$ . For compounds whose thermodynamic data is not included in the FACTSAGE 5.4 database, calculation of the Gibbs free energy change was processed separately by using values collected from the literature.

## 3. Results

### 3.1. Electrochemical testing

#### 3.1.1. SOFC performance in pure fuels

Fig. 2 shows plots of cell voltage and power density versus current density for a typical LSFerCr–GDC anode SOFC operated at  $800^\circ\text{C}$  in various fuel compositions and constant air flow of 300 sccm. The OCVs were  $\approx 1.08\text{ V}$  in dry  $H_2$  and  $1.06\text{ V}$  in  $97\%H_2/3\%H_2O$ . The latter value was slightly lower than the the-

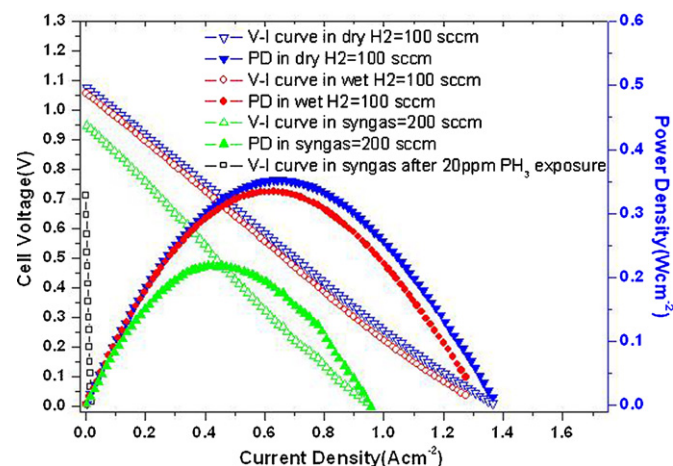


Fig. 2. Cell performances as a function of feed fuel composition (CG-P20).

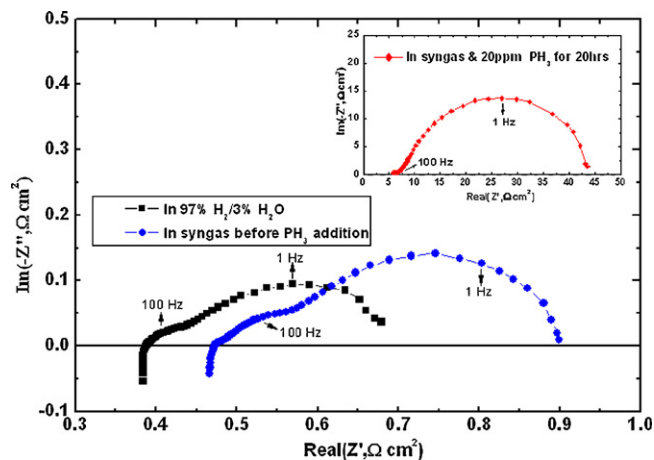


Fig. 3. AC impedance spectra at OCV of CG-P20 tested in  $97\%H_2/3\%H_2O$  and simulated coal syngas before/after  $PH_3$  addition.

oretical value of  $1.10\text{ V}$  for wet hydrogen, but slightly higher than measured OCV in wet  $H_2$  previously for similar SOFCs [14]. Thus, gas leakage across the compressive mica sealant was relatively minor. After switching the fuel to the surrogate syngas composition ( $30\%H_2$ ,  $26\%H_2O$ ,  $23\%CO$  and  $21\%CO_2$ ), the OCV dropped to  $0.948\text{ V}$ , in good agreement with the theoretical OCV value of  $0.949\text{ V}$  expected at  $800^\circ\text{C}$ . The maximum power density ranged from  $355\text{ mW cm}^{-2}$  with 100 sccm of dry  $H_2$ , to  $341\text{ mW cm}^{-2}$  with 100 sccm of wet  $H_2$ , and  $218\text{ mW cm}^{-2}$  with 200 sccm of syngas fuel. These results were typical of the cells measured in this study, and similar to previously reported results for similar SOFCs [14]. Only one of the cells tested showed inferior performance, and this was not used in the results below.

AC impedance Nyquist plots from a cell measured at OCV with syngas and wet  $H_2$  are shown in Fig. 3. The high-frequency real-axis intercept increased from  $0.39\ \Omega\text{ cm}^2$  to  $0.47\ \Omega\text{ cm}^2$  when the fuel was switched from  $H_2$  to coal syngas. The impedance spectra showed two characteristic arcs at  $\sim 10^2\text{ Hz}$  and  $\sim 10^0\text{ Hz}$  that were attributed to the anode because prior studies on these cells suggested that the cathode resistance was relatively small [14]. The lower frequency electrode arc dominated the impedance spectra, similar to the result reported previously for cells with the LSFerCr–GDC anode. The overall cell polarization resistance ( $R_p$ ) increased from  $0.32\ \Omega\text{ cm}^2$  to  $0.43\ \Omega\text{ cm}^2$  on switching to coal gas.

#### 3.1.2. SOFC performance in fuels containing $PH_3$

Fig. 4 shows cell voltage versus time at a fixed current density of  $0.25\text{ A cm}^{-2}$  for cells operated in 200 sccm of simulated coal syngas with and without 20 ppm  $PH_3$  impurity. Both cells had been operated in wet  $H_2$  with a constant current load of  $0.25\text{ A cm}^{-2}$  prior to the coal gas testing shown. The cell operated in clean coal syngas showed an initial voltage of  $0.68\text{ V}$  that decreased slightly before stabilizing at  $\approx 0.64\text{ V}$ . No significant performance/structural degradation was observed in this cell during post-test characterization, indicating that the LSFerCr–GDC composite oxide was generally stable during syngas operation. The other cell was first tested in phosphine-free syngas for 24 h, during which time it displayed good stability. However, 4 h after the introduction of 20 ppm  $PH_3$  into the syngas, the cell voltage began to drop rapidly, reaching zero in  $<5\text{ h}$ . The cell performance did not recover after removing the  $PH_3$  from the fuel supply. The inset in Fig. 3 shows the AC impedance spectrum measured after the cell failure. Both  $R_s$  and  $R_p$  increased by orders of magnitude after  $PH_3$  exposure, indicating that the perovskite anode had lost both its conductivity and electrocatalytic activity.

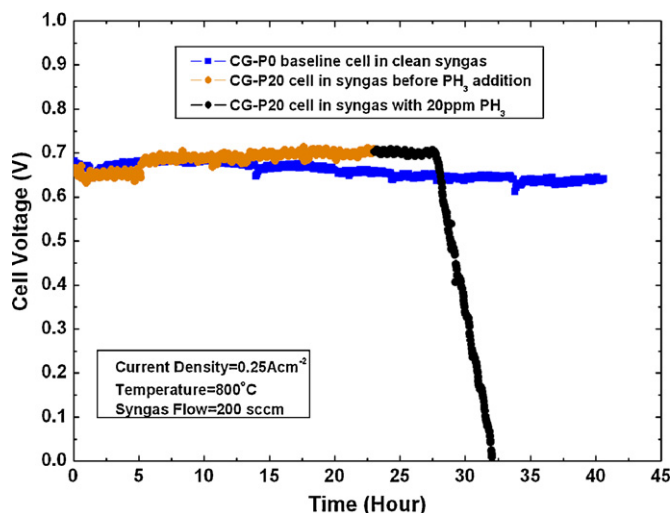


Fig. 4. Cell voltage change in syngas for a baseline cell (CG-P0) and cell poisoned by 20 ppm  $\text{PH}_3$  (CG-P20).

Additional life tests were carried out with wet  $\text{H}_2$  fuel laden with 5 ppm and 20 ppm  $\text{PH}_3$ . Fig. 5 shows that both cells operated stably in the wet  $\text{H}_2$ . Similar to Fig. 4, the cells continued to operate stably for several hours after introduction of  $\text{PH}_3$  but then rapidly degraded. For 20 ppm, the delay was  $\sim 4$  h; comparison with Fig. 4 indicates that the fuel composition ( $\text{H}_2$  or coal gas) did not affect the time before rapid degradation. For 5 ppm, the stable cell performance was sustained for a longer period of 7 h after contaminant introduction, and the subsequent degradation occurred at a slower rate  $-96 \text{ mV h}^{-1}$  versus  $-65 \text{ mV h}^{-1}$  for 20 ppm. In both cases, the cell performance did not recover after removing the  $\text{PH}_3$ . Thus, the anode was destroyed by both  $\text{PH}_3$  concentrations, but the degradation took longer for the lower  $\text{PH}_3$  level.

Fig. 6 presents the AC impedance spectra taken at 5 h, 6 h, 18 h and 20 h after the introduction of 5 ppm  $\text{PH}_3$ , as indicated by the arrows in Fig. 5. The spectra taken 5 h and 6 h after  $\text{PH}_3$  introduction were only slightly changed from the pre- $\text{PH}_3$  spectrum. The primary change was an increase in the high-frequency intercept. In contrast, after serious cell degradation (18 h and 20 h after  $\text{PH}_3$  introduction), both  $R_s$  and  $R_p$  were substantially larger.

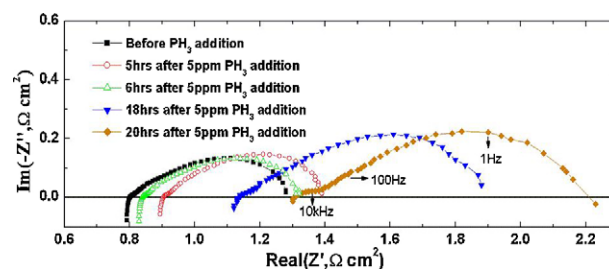


Fig. 6. AC impedance change at OCV of H2-P5 cell tested in 97% $\text{H}_2$ /3% $\text{H}_2\text{O}$  before/after 5 ppm  $\text{PH}_3$  addition

## 3.2. Material characterization

### 3.2.1. XRD analysis

XRD patterns were recorded from the anodes after cell testing in order to identify changes in the phases present. In each case with  $\text{PH}_3$  exposure, the test was continued until the cell voltage went to zero, as illustrated in Fig. 5. Fig. 7 shows the XRD patterns for an un-tested anode and cells tested in wet hydrogen and exposure to 5 ppm  $\text{PH}_3$  for 22 h and to 20 ppm  $\text{PH}_3$  for 15 h. The humidified  $\text{H}_2$  case showed only the expected phases – LSCr, GDC, and LSGM – along with Au from the anode current collectors. After  $\text{PH}_3$  exposure, additional XRD reflections were observed and tentatively identified as new oxide ( $\text{FeO}$ ,  $\text{Fe}_2\text{O}_3$ ,  $\text{Sr}_2\text{CrO}_4$ , and  $\text{P}_2\text{O}_5$ ), phosphate ( $\text{LaPO}_4$  and  $\text{FePO}_4$ ), and phosphide ( $\text{FeP}$ ) phases. The strongest peaks were those identified as  $\text{FeP}$ ,  $\text{FeO}$ ,  $\text{Fe}_2\text{O}_3$ ,  $\text{FePO}_4$ ,  $\text{Sr}_2\text{CrO}_4$  and  $\text{P}_2\text{O}_5$ . Note that there was considerable overlap of the various impurity phase reflections, such that these identifications have some uncertainty. Note that intensity from the Pt current collector (peaks appearing at  $39.7^\circ$ ,  $46.2^\circ$  and  $67.4^\circ$ ) may also have been present, but a definitive identification could not be made since these overlapped with other peaks. The results for the two  $\text{PH}_3$  concentrations were similar, except that the main peaks belonging to  $\text{FeP}$  and  $\text{LaPO}_4$  were slightly stronger at the higher concentration of  $\text{PH}_3$  (20 ppm), while the  $\text{P}_2\text{O}_5$  and  $\text{FePO}_4$  peaks were slightly less prominent. Substantially increased product formation would be expected at higher  $\text{PH}_3$  concentrations, but was probably mitigated by the 0.5 times shorter 20 ppm exposure compared to the

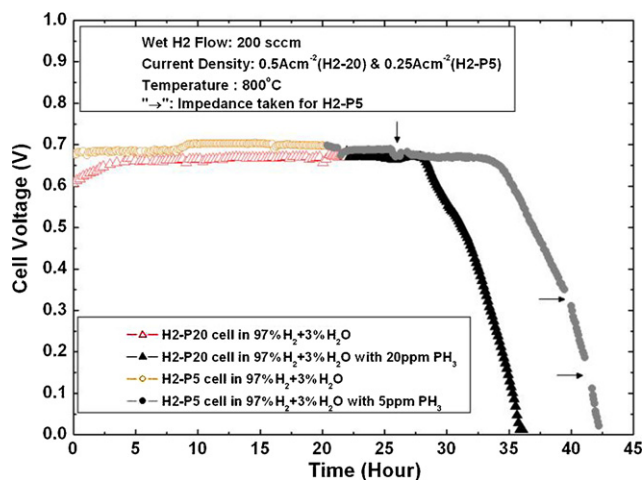


Fig. 5. Cell voltage change in 97% $\text{H}_2$ /3% $\text{H}_2\text{O}$  for cells poisoned by 20 ppm  $\text{PH}_3$  (H2-P20) and by 5 ppm  $\text{PH}_3$  (H2-P5).

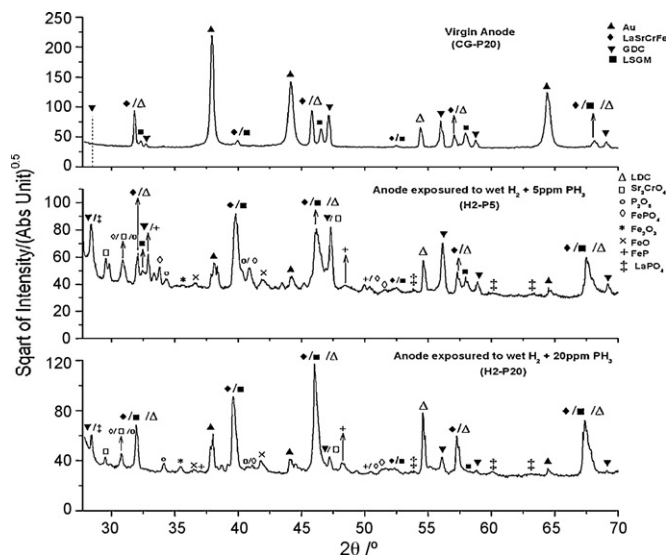


Fig. 7. XRD spectra of cells tested with 97% $\text{H}_2$ /3% $\text{H}_2\text{O}$  and different levels of  $\text{PH}_3$  impurity.

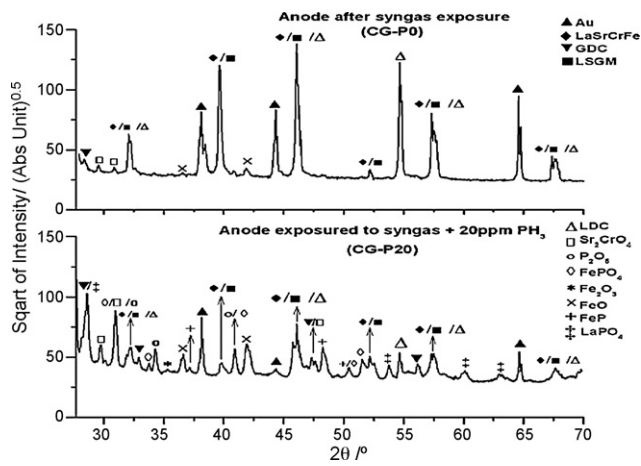


Fig. 8. XRD spectra of cells tested in syngas with and without PH<sub>3</sub> impurity.

5 ppm exposure time. No phases were detected that would indicate reactions of Pt or Au with phosphorus, indicating that the current collector did not degrade in the presence of PH<sub>3</sub>.

Fig. 8 displays the XRD spectra for cells tested in syngas. After syngas exposure for 40 h, peaks corresponding to Sr<sub>2</sub>CrO<sub>4</sub> were detected, and weak peaks identified as FeO were also present. This showed that a slight anode phase evolution occurred during the syngas operation, although there was no apparent effect on anode electrical performance (Fig. 4). For the CG-P-20 cell operated in syngas with 20 ppm PH<sub>3</sub>, all the peaks of impurity phases belonging to the phosphides and phosphates previously identified for cells operated in H<sub>2</sub> and PH<sub>3</sub> were sharper and clearer, and the perovskite peaks were weaker. Thus, the anode reaction may have been more complete for PH<sub>3</sub> exposure in syngas compared to hydrogen.

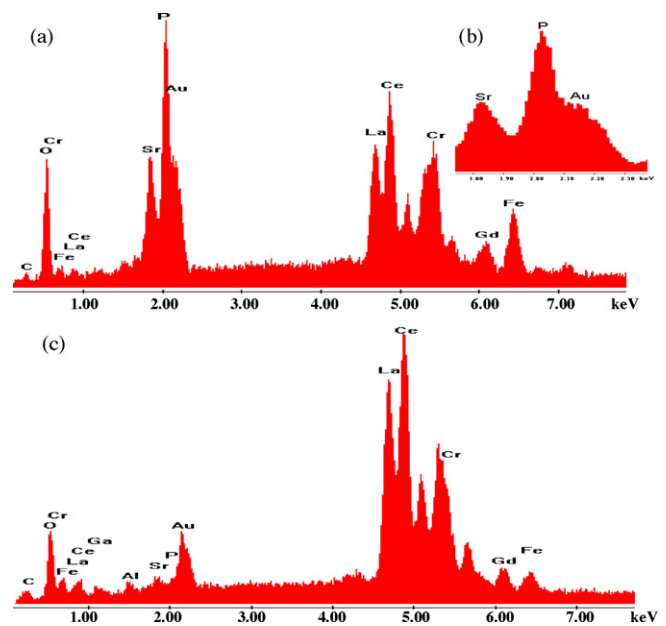


Fig. 10. Cross-section EDS spectra of H<sub>2</sub>-P5 cell after 5 ppm PH<sub>3</sub>-poisoning in 97%H<sub>2</sub>/3%H<sub>2</sub>O recorded at (a) the LSFerCr–GDC anode and (c) near the LDC layer. The inset (b) is a close-up of the P(Kα) and Au(Mα) line position.

3.2.2. SEM and EDX analysis

Fig. 9 shows cross-sectional SEM images of the anodes after tests. It can be found that anodes exposed to 20 ppm PH<sub>3</sub> in either H<sub>2</sub> (Fig. 9b) or syngas (Fig. 9c) had become densified as compared to the one exposed to 5 ppm PH<sub>3</sub> (Fig. 9a), a change presumably associated with the various reactions and new phases shown in Figs. 7 and 8.

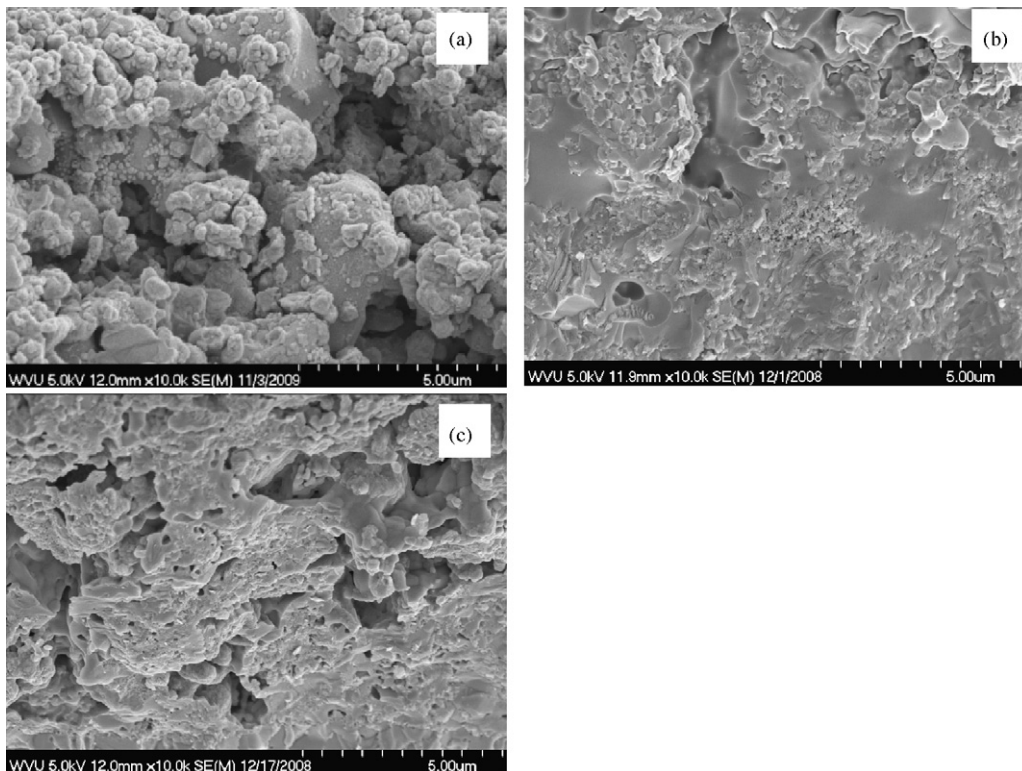


Fig. 9. Cross-sectional SEM pictures of a cell (a) anode operated in wet H<sub>2</sub> with 5 ppm PH<sub>3</sub>, (b) anode operated in wet H<sub>2</sub> with 20 ppm PH<sub>3</sub>, (c) anode operated in syngas with 20 ppm PH<sub>3</sub>.

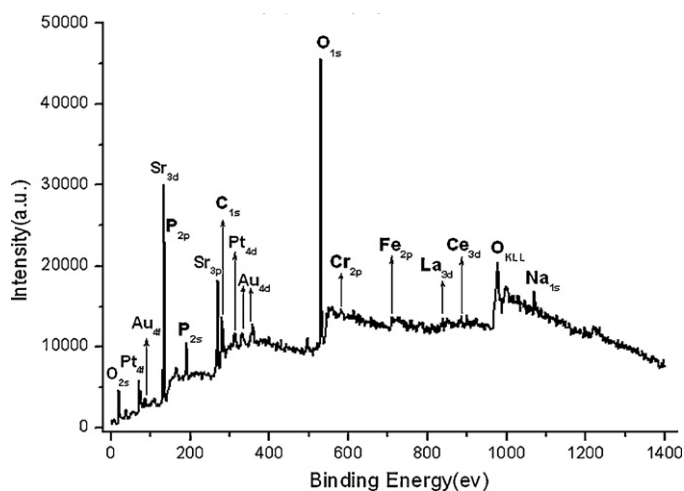


Fig. 11. XPS spectra of a survey scan of the H2-P5 cell anode surface after 5 ppm PH<sub>3</sub> testing in 97%H<sub>2</sub>/3%H<sub>2</sub>O.

Fig. 10 shows EDS spectra obtained from the cross-sectioned surfaces of the anode layer (a and b) and the LDC interlayer (c) after operation in 5 ppm PH<sub>3</sub>. The spectra showed all of the expected peaks in each case, with the addition of a strong P peak in the anode layer. The inset shows a magnified view of the region around the P peak, clarifying that a strong P peak was indeed present. On the other hand, only a trace amount of P was observed in the LDC interlayer, in agreement with the above XRD results that showed no change of LDC peak before and after PH<sub>3</sub> testing.

### 3.2.3. XPS analysis

Fig. 11 shows a survey XPS spectrum from the anode that had been tested in 5 ppm PH<sub>3</sub> in H<sub>2</sub>. Again, peaks are identified from each of the anode constituents, along with P. The O 1s, Sr 3d and P 2p peaks were relatively strong compared to the Fe 2p, Cr 2p, La 3d and Ce 3d peaks; taking into account the elemental sensitivities from the XPS handbook, this suggests that the anode surface was enriched with Sr and P. The P 2p peaks were overlapped with the Sr 3d peaks at 130–135 eV, but the presence of surface P and Sr were confirmed separately by the P 2s and Sr 3p peaks.

Fig. 12 shows magnified views of the 130–135 eV region for the anode tested in 20 ppm PH<sub>3</sub> in syngas (Fig. 12a) along with the 5 ppm PH<sub>3</sub> in H<sub>2</sub> case (Fig. 12b). The Sr 3d and P 2p peaks combined to yield an apparent double peak. Fig. 12 also shows that excellent fits to the combined Sr/P peaks were obtained in both cases by deconvoluting the spectra into coupled electron peaks, using the Multipack XPS software carried by the Versa Probe testing system. The identified peak positions for P 2p and Sr 3d high-spin electrons are listed in Table 2.

The P 2p<sub>3/2</sub> electron in the XPS spectrum for the anode poisoned by 5 ppm PH<sub>3</sub> showed binding energies of 133.7 eV, which corresponded well to the phosphorous state in phosphate, according to the NIST XPS database [17]. For the 20 ppm PH<sub>3</sub> case two valence states were identified for surface phosphorus with binding energies of 133.4 eV (P1) and 131.4 eV (P2). The former value indicates a phosphate state, while the latter value falls between that of FeP (129.5 eV) and the reported value for oxidized phosphorus in

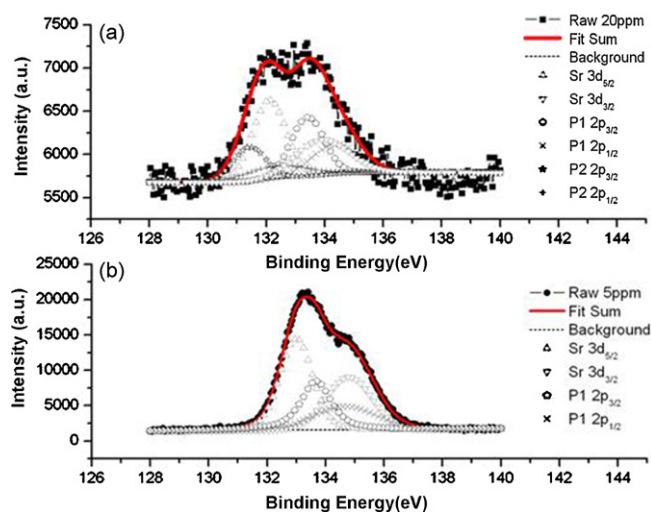


Fig. 12. Original (raw) and deconvoluted Sr3d and P2p XPS spectra for an (a) anode after exposure to 20 ppm PH<sub>3</sub> in simulated syngas (CG-P20) and (b) anode after exposure to 5 ppm PH<sub>3</sub> testing in 97%H<sub>2</sub>/3%H<sub>2</sub>O (H2-P5).

a phosphide (132.7 eV). Phosphorous oxidation may have resulted from exposure of the sample to air after testing [18]. Preservation of the lower electron state for phosphorus in the sample exposed to 20 ppm PH<sub>3</sub> may have resulted from enhanced reaction with the perovskite anode due to higher PH<sub>3</sub> concentration. Additionally, exposure of the 20 ppm sample to hydrogen during the attempt to recover cell performance likely contributed to the formation of low-valence phosphorus in the sample.

The Sr 3d<sub>5/2</sub> peak in the spectrum of the 5 ppm PH<sub>3</sub>-poisoned anode was located at 133.0 eV, close to the reported value of the Sr cation in perovskite oxides [19]. This peak shifted to a lower binding energy of 132.1 eV in the spectrum for the anode exposed to 20 ppm PH<sub>3</sub>, in agreement with Sr found in SrO<sub>1-x</sub> (132.2 eV) [20]. A similar valence state change for the Fe cation was observed in Fig. 13, where the binding energies corresponding to the Fe 2p<sub>3/2</sub> and 2p<sub>1/2</sub> electrons also became smaller for the 20 ppm PH<sub>3</sub>-poisoned anode compared to the 5 ppm case. In general, for higher PH<sub>3</sub> concentration, the valence state change of Sr and Fe cations may be related to the increased reaction of metal components in the perovskite structure with higher concentration of phosphorus at the anode surface, as electron binding energy tends to decrease when such metal ions bond with P, with lower electronegativity than oxygen.

## 4. Discussion

The results presented above indicated that PH<sub>3</sub> impurity at ppm levels severely degrades the performance of LSFerCr SOFC anodes. Structural/chemical analysis in Section 3 indicated the formation of new phosphide and phosphate phases and decomposition of the perovskite phase were accompanied by a densification of the anode. The structural/chemical measurements were all taken after cell tests in which the anode was exposed to PH<sub>3</sub> until the cell voltage dropped to zero. This suggests that the degradation was nearly complete, *i.e.*, that the anode was approaching its equilibrium com-

Table 2  
P 2p, Sr 3d and Fe 2p XPS peaks of anodes after exposure to 5 ppm and 20 ppm PH<sub>3</sub>.

Sample	Peak position			
	P 2p <sub>3/2</sub> peak 1 (eV)	P 2p <sub>3/2</sub> peak 2 (eV)	Sr 3d <sub>5/2</sub> peak (eV)	Fe 2p <sub>3/2</sub> peak (eV)
CG-P20 (20 ppm PH <sub>3</sub> )	133.4	131.4	132.1	709.5
H2-P5 (5 ppm PH <sub>3</sub> )	133.7	–	133.0	712.1

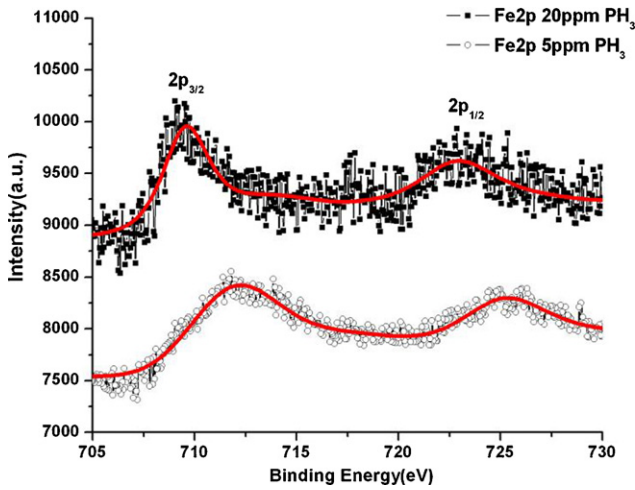


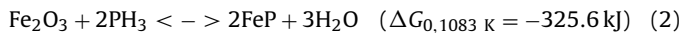
Fig. 13. Comparison of Fe2p XPS spectra of the H2-P5 cell anode and CG-P20 cell anode after PH<sub>3</sub> testing in 97%H<sub>2</sub>/3%H<sub>2</sub>O.

position and phase distribution. Thus, it should be reasonable to compare the experimental results with thermodynamic predictions, at least qualitatively.

In the following, a thermodynamic analysis of the stable phases expected in PH<sub>3</sub> is described (Section 4.1). The degradation mechanisms are then discussed in light of the thermodynamic results (Section 4.2), and compared with Ni-YSZ (Section 4.3).

#### 4.1. Thermodynamic calculations

The thermodynamic calculation aimed to determine the conditions under which different phases were expected to form. Given the above XPS and XRD results, where the new phases identified included Fe phosphides and phosphates, the calculations focused on determining the Fe phases expected at varying PH<sub>3</sub> concentrations and fuel oxygen partial pressure. The possible phosphide formation reactions between Fe and PH<sub>3</sub> are:



The Gibbs free energy changes were calculated by FACTSAGE. Figs. 14 and 15 show the Fe–PH<sub>3</sub>–O<sub>2</sub> predominance phase diagrams

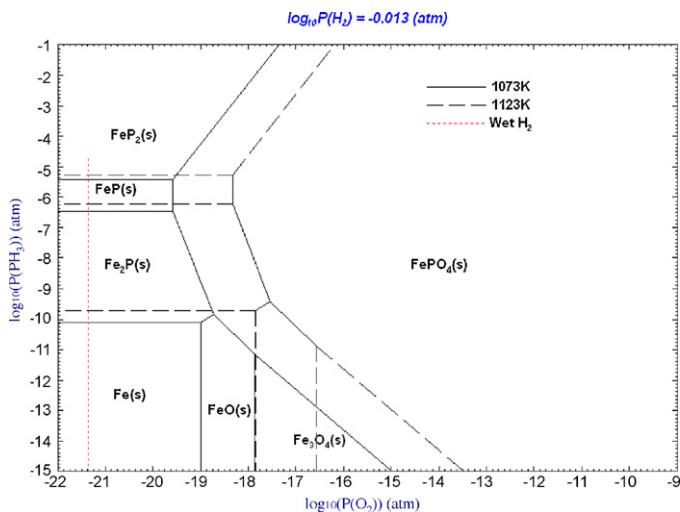


Fig. 14. Predominant phase diagrams of Fe–P–O–H system at 800°C and 850°C, assuming PH<sub>3</sub> as reactant and  $p_{\text{H}_2} = 0.97$  bar.

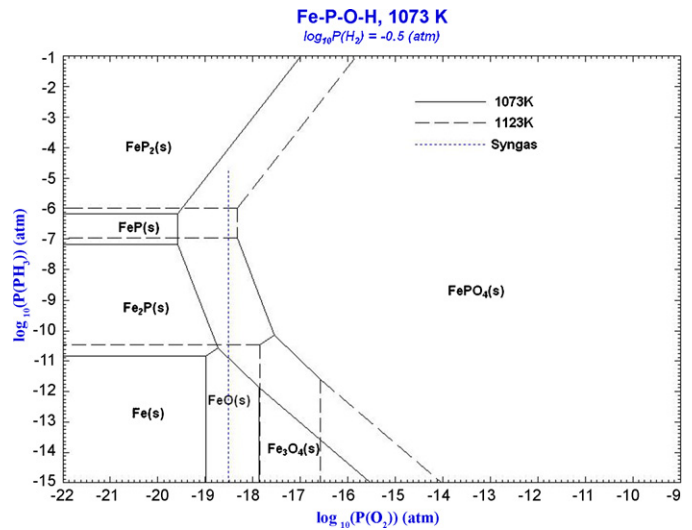


Fig. 15. Predominant phase diagrams of Fe–P–O–H system at 800°C and 850°C, assuming PH<sub>3</sub> as reactant and  $p_{\text{H}_2} = 0.31$  bar.

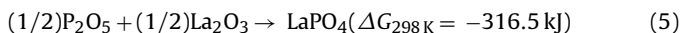
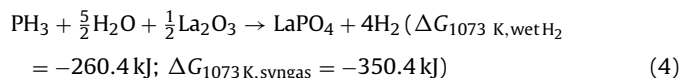
that were calculated using the FACTSAGE software for the surrogate syngas and wet H<sub>2</sub> respectively. For the conditions of the present H<sub>2</sub>/H<sub>2</sub>O experiments (Fig. 14) – PH<sub>3</sub> pressure of  $5 \times 10^{-6}$  atm or  $2 \times 10^{-5}$  atm,  $T = 1073$  K, and an effective oxygen partial pressure of  $10^{-21.38}$  atm (wet H<sub>2</sub>) – the predicted phosphide phase was FeP for 5 ppm PH<sub>3</sub> test and FeP<sub>2</sub> for 20 ppm PH<sub>3</sub>, although the experimental conditions were close to the FeP/FeP<sub>2</sub> phase boundary. In contrast, only FeP was observed experimentally by XRD; this discrepancy may be due to the approximate nature of the calculation results, where Fe was assumed to be present as pure Fe or Fe<sub>2</sub>O<sub>3</sub>, rather than in the perovskite phase. In the syngas atmosphere, the oxygen partial pressure was higher,  $P_{\text{O}_2} = 10^{-19} - 10^{-18}$  atm as labeled in Fig. 15, such that FePO<sub>4</sub>(s) could form.

Fig. 15 predicts that increasing the PH<sub>3</sub> concentration above ~100 ppm will favor the existence of FeP<sub>2</sub> over FeP and FePO<sub>4</sub>. The results also indicate that the PH<sub>3</sub> concentration would have to be reduced to quite low values, <1 ppb, in order to avoid the formation of phosphate or phosphide phases. The calculated results for 1123 K, also shown in Fig. 15, indicated that the phosphide region extends to higher  $P_{\text{O}_2}$  at higher temperature. These predictions are not in complete agreement with the XRD results that showed both phosphide and phosphate phases. However, the phosphide is less stable at lower temperatures. Thus, the post-test XRD results may reflect the tendency for phosphide to become oxidized during cooling at the end of the cell testing. Note that the cells were cooled from 800°C to room temperature in N<sub>2</sub> within 2–3 h. This may explain the presence of Fe<sub>2</sub>O<sub>3</sub> with FeP in the XRD data. Under this more oxidizing condition and with PH<sub>3</sub> no longer present, it is reasonable to expect partial oxidation of the FeP. This was previously observed under similar conditions for the case of nickel phosphide formation [5].

LaPO<sub>4</sub> was also identified in the present XRD scans. This is similar to a prior report where the conversion of a LaCoO<sub>3</sub> perovskite catalyst to LaPO<sub>4</sub> and La<sub>4</sub>(P<sub>2</sub>O<sub>7</sub>)<sub>3</sub> secondary phases were observed as a result of organophosphorus exposure in Ar atmosphere [21]. The lack of thermodynamic data in the FACTSAGE database prevented calculation of the predominant phase diagram for the La<sub>2</sub>O<sub>3</sub>–PH<sub>3</sub> system as a function of oxygen partial pressure and PH<sub>3</sub> concentration. Thermodynamic data for possible LaPO<sub>4</sub> formation reactions [22,23] was thus used to calculate the Gibbs free energy change ( $\Delta G$ ) of the reaction using:

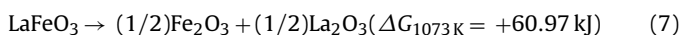
$$\Delta G = \Delta G_{0,T} + RT \ln K \quad (3)$$

where  $T$  is temperature,  $R$  is the gas constant, and  $K$  the equilibrium constant. The standard Gibbs free energy change ( $\Delta G_{0,T}$ ) was calculated from the formation enthalpy and entropy of each compound involved in the reaction, and then substituted stoichiometrically into Eq. (3) to calculate  $K$  to get the overall Gibbs free energy change. The resulting values with  $2 \times 10^{-5}$  atm  $\text{PH}_3$  are:



The calculation was based upon the assumption which views the perovskite structure as a solution composed of simple oxides, which has been adopted in other research on stability of the perovskite anode [24]. The results showed that the formation of the  $\text{LaPO}_4$  phase at  $800^\circ\text{C}$  is quite energetically favorable, and that  $\text{LaPO}_4$  is a thermodynamically stable phase at testing conditions. Additionally, the formation of  $\text{LaPO}_4$  is expected to be more favorable in the syngas atmosphere than in wet  $\text{H}_2$ . The sample exposed to 20 ppm  $\text{PH}_3$  in syngas did appear to degrade faster than the one tested in wet  $\text{H}_2$  with same  $\text{PH}_3$  concentration. In addition, Eq. (5) indicates that  $\text{LaPO}_4$  can also be produced at room temperature from reaction of  $\text{P}_2\text{O}_5$  and  $\text{La}_2\text{O}_3$ , thus a more detailed study would be required to identify the true reaction mechanism of  $\text{La}_2\text{O}_3$  in perovskite with  $\text{PH}_3$ .

An important question is whether  $\text{LaPO}_4$  forms because the perovskite phase is first de-stabilized by the loss of Fe to  $\text{FeP}$ , or whether it would form from a stable perovskite. Thus additional calculations were completed to estimate the stability of the present perovskite structure under exposure to  $\text{PH}_3$  at cell operating conditions. The characteristic thermodynamic data of  $\text{LSFeCr}$  perovskite is unknown, hence stability of the anode was estimated by using thermodynamic data recently reported for the simple perovskite systems as  $\text{LaCrO}_3$  and  $\text{LaFeO}_3$  [25,26]. The Gibbs free energy change for dissociation reactions of the above perovskites were calculated as follows:



The combined Gibbs free energy change for reactions (4) and (6) together to form  $\text{LaPO}_4$  would be  $-184.35\text{ kJ}$  and  $-274.35\text{ kJ}$  respectively for wet  $\text{H}_2$  and syngas. The values for the  $\text{LaFeO}_3$  system would be more negative considering further reaction of  $\text{Fe}_2\text{O}_3$  with  $\text{PH}_3$ . Therefore, the above calculation shows it is energetically favorable for the La and Fe, and La and Cr containing perovskite system to decompose under  $\text{PH}_3$  attack and form  $\text{LaPO}_4$ . Experiments with  $(\text{La,Sr})\text{CrO}_3$  anodes will be useful to identify the reactions between La and  $\text{PH}_3$ . The results will be reported later.

Finally, a thermodynamic analysis similar to that outlined above was performed to examine possible reactions between  $\text{Cr}_2\text{O}_3$  and  $\text{PH}_3$ . It was found that no reaction was expected for the present test conditions. This agrees with the present XRD results that showed no Cr phosphides or phosphates. Although a new  $\text{Sr}_2\text{CrO}_4$  phase was observed, this may have formed as a result of the loss of La and Fe from the original  $\text{LSFeCr}$  perovskite phase.

#### 4.2. Anode reaction and degradation mechanisms

While the above thermodynamic predictions provided good agreement with the XRD results, they provided little information about the reaction sequence. It seems reasonable to suggest that La and Fe reacted with  $\text{PH}_3$ , with the result that the perovskite phase decomposed, either directly to the phosphides/phosphates or via intermediates such as  $\text{Sr}_2\text{CrO}_4$  (observed by XRD) or  $\text{SrO}$  (observed by XPS).

The electrical testing results showed that the rapid cell degradation occurred only after 4–7 h of  $\text{PH}_3$  exposure. EIS data (Fig. 6) taken during the initial period of stable performance showed only a slight increase in the first real-axis intercept, which was mainly due to the LSGM electrolyte. However, slight variations in the cell performance with time were also observed for cells tested without  $\text{PH}_3$ , so this change was not necessarily associated with anode poisoning. The cell polarization resistance did not change, indicating that the active anode surfaces or three-phase boundaries were not poisoned by  $\text{PH}_3$ .

The delay prior to the rapid degradation could have a few explanations. First, there may have been an incubation time prior to nucleation of the new phosphide or phosphate phases. Second, the growth of the new phases may have been relatively slow, such that it took some time before sufficient  $\text{LSFeCr}$  was consumed to deleteriously affect electrochemical processes. Prior studies have shown that the out-diffusion of cation species from chromite anode particles, *i.e.*, Ru out of  $\text{La}_{0.8}\text{Sr}_{0.2}\text{Cr}_{0.82}\text{Ru}_{0.18}\text{O}_{3-\delta}$  [27] occur over several hours at SOFC operating conditions. This process could have limited the phosphide/phosphate growth rate. Another possibility is that the reaction occurred first at the outer surfaces of the anode, having little impact on anode function until the reaction front approached the electrolyte. Finally, the reaction may have been limited by the supply of  $\text{PH}_3$ . Given that the anode was  $20\text{ }\mu\text{m}$ -thick,  $0.5\text{ cm}^2$  in area,  $\sim 33\%$   $\text{LSFeCr}$  by volume, and the density of  $\text{LSFeCr}$  is  $\approx 6\text{ g cm}^{-3}$ ; there was  $2.0\text{ mg}$  of  $\text{LSFeCr}$  ( $0.36\text{ mg Fe}$ ,  $0.45\text{ mg La}$ ) in the anode. Thus,  $\approx 0.8\text{ mg}$  of P would be needed to react with these species according to the above phosphide or phosphate formation reactions. At a flow rate of 200 sccm with 5 ppm  $\text{PH}_3$ , the molar  $\text{PH}_3$  flow rate is  $4.16 \times 10^{-8}\text{ moles min}^{-1}$  or  $1.3\text{ }\mu\text{g P/min}$ . At this rate, it would take 620 [230 min] min to fully react the La and Fe in the anode if a fraction of the fuel does not interact with the anode in the test rig, in agreement with the time observed for complete anode failure. For the 20 ppm  $\text{PH}_3$  case, the predicted time is reduced to 155 [58 min] min, again in reasonable agreement with the observed degradation times. These estimates suggest that  $\text{PH}_3$  is extremely reactive with  $\text{LSFeCr}$ , such that the reaction is limited mainly by the supply of  $\text{PH}_3$ .

During the rapid degradation stage, both the ohmic and polarization resistance portions of the EIS increased rapidly. This is readily explained by the consumption of  $\text{LSFeCr}$ , which eliminated surfaces and three-phase boundaries that contributed to electrochemical reactions, reduced the extrinsic anode conductivity, and disrupted/densified the anode structure due to volume changes from phosphide/phosphate formation.

#### 4.3. Comparison with Ni-YSZ anodes

The present results can be compared directly with a recent report on the operation of Ni-YSZ anode-supported SOFCs on syngas containing 10 ppm  $\text{PH}_3$  [5]. A striking difference is the much slower degradation of the Ni-YSZ anodes ( $\approx 0.5\text{ mV h}^{-1}$ ) compared to the present anodes ( $\approx 100\text{ mV h}^{-1}$ ). This is despite the higher reactivity of Ni with  $\text{PH}_3$ ; thermodynamic predictions suggested that nickel phosphides form at  $\text{PH}_3$  partial pressures down to  $10^{-13}$  atm compared to  $10^{-11}$  atm for the  $\text{LSFeCr}$  anodes. A likely explanation for the much slower Ni-YSZ anode degradation rate was the much larger amount of Ni,  $\sim 330\text{ mg cm}^{-2}$  or  $\sim 400$  times the amount of La and Fe in the present anodes. The calculation in the prior section indicated that the rate of anode phosphidization was limited by the supply of  $\text{PH}_3$ . Thus, the larger amount of Ni resulted in a much slower degradation rate.

One might also suggest that Fe being in the stable perovskite oxide might lend it greater stability against  $\text{PH}_3$  attack compared to a metallic phase such as Ni. However, it has been noted previ-

ously that Fe in LSCr is barely stable under SOFC anode conditions compared to metallic Fe. Thus, the activities of Fe in the metallic and perovskite phases must be similar, and hence they should have similar reactivities with  $\text{PH}_3$ .

## 5. Summary and conclusions

The performance and stability of LSGM-electrolyte supported SOFCs with LSCr–GDC composite anodes were studied in coal syngas and wet  $\text{H}_2$  fuels containing phosphine impurity. Several conclusions can be drawn and future work is suggested.

1. Introduction of 5–20 ppm  $\text{PH}_3$  into the fuels caused complete cell performance degradation within 11–24 h, with no recovery after removing  $\text{PH}_3$  impurity from the fuels.
2. There was an initial period of 4–7 h where there was little change in cell electrochemical performance, followed by a very rapid decline in cell voltage at constant current. This suggests that impurity-related chemisorbed species did not interfere with electrochemical reactions.
3. Rather, the degradation was associated with a decomposition of the LSCr perovskite structure, with the formation of new phases including FeP,  $\text{FePO}_4$ ,  $\text{LaPO}_4$ , and  $\text{Sr}_2\text{CrO}_4$ . It seems likely that the perovskite phase was de-stabilized by the removal of Fe to form FeP and/or  $\text{FePO}_4$ . It is not clear whether  $\text{LaPO}_4$  would form from an otherwise stable perovskite, such as  $(\text{La,Sr})\text{CrO}_3$ . This is an important question to be answered in future work, as it will establish whether La-based anodes can be useful P-tolerant anodes.
4. The present results, combined with prior work on Ni-YSZ, suggest that anodes containing transition metals that are highly reactive with P will not be stable in ppm levels of  $\text{PH}_3$ . Preliminary thermodynamic calculations suggest that Mn may be a better choice than Fe because it is less reactive, the critical  $\text{PH}_3$  partial pressure to form a phosphide was much higher,  $\sim 100$  ppm. Thus materials such as  $(\text{La,Sr})(\text{Cr,Mn})\text{O}_3$  and  $\text{Sr}(\text{Mn,Mo,Mg})\text{O}_3$  should probably be tested with  $\text{PH}_3$ -containing fuels.
5. Thermodynamic calculations were in reasonable agreement with the experimental observations, predicting FeP,  $\text{FeP}_2$ ,  $\text{FePO}_4$ , and  $\text{LaPO}_4$  as stable reaction products under the SOFC anode test conditions. The calculations also indicated that phosphide/phosphate formation was expected even for 1 ppb  $\text{PH}_3$  concentrations. Thus, it seems likely that similar degradation will occur at the  $\text{PH}_3$  concentrations expected in coal syngas (1–2 ppm), that are slightly lower than in the present experiments.
6. The time to anode failure, which increased for lower  $\text{PH}_3$  concentration, agreed well with the time required to supply sufficient  $\text{PH}_3$  to fully react with the La and Fe in the anode. This shows that the LSCr was extremely reactive with  $\text{PH}_3$ .

## Acknowledgements

WVU part of this work is sponsored by US Department of Energy EPSCoR Program under grant number DE-FG02-06ER46299. Dr. Tim Fitzsimmons is the DOE Technical Monitor. Dr. R. Bajura is the Administrative Manager and Dr. I. Celik is the Technical Manager and Principal Investigator of WVU EPSCoR project. The work at Northwestern University was sponsored by the Department of Energy under Award Number DE-FG02-05ER46255. The authors would like to thank Dr. Randall S. Gemmen from National Energy Technology Lab for his technical advice and allowing us to use FACTSAGE software. Dr. Andy Woodworth, Mr. Liviu Magean, and Mrs. Adrienne McGraw are acknowledged for operation of SEM, EDX, XRD and XPS analysis.

## References

- [1] M.C. Williams, J. Strakey, W. Surdoval, J. Power Sources 159 (2006) 1241–1247.
- [2] R.S. Gemmen, J.P. Trembly, J. Power Sources 161 (2) (2006) 1084–1095.
- [3] J.P. Trembly, R.S. Gemmen, D.J. Bayless, J. Power Sources 163 (2007) 986–996.
- [4] O.A. Marina, L.R. Pederson, D.J. Edwards, C.W. Coyle, J. Templeton, M. Engelhard, Z. Zhou, Proceedings of the 8th SECA Annual Workshop, San Antonio, TX, 2007.
- [5] C. Xu, J.W. Zondlo, H.O. Finkler, O. Demircan, M. Gong, X. Liu, J. Power Sources 193 (2) (2009) 739–746.
- [6] F.N. Cayan, M. Zhi, S.R. Pakalapati, I. Celik, N.Q. Wu, R.S. Gemmen, J. Power Sources 185 (2) (2008) 595–602.
- [7] L. Aguilar, S. Zha, Z. Cheng, J. Winnick, M. Liu, J. Power Sources 135 (1) (2004) 17–24.
- [8] J.P. Trembly, D.J. Bayless, R.S. Gemmen, Symposium of 23rd International Pittsburgh Coal Conference, Pittsburgh, PA, 2006.
- [9] R. Munkundan, E.L. Brosha, F.H. Garzon, Electrochem. Solid State Lett. 7 (1) (2004) A5–A7.
- [10] O.A. Marina, SECA Core Technology Program Peer Review, Boston, MA, 2004.
- [11] S.W. Tao, J.T.S. Irvine, Chem. Mater. 16 (21) (2004) 4116–4121.
- [12] S.W. Tao, J.T.S. Irvine, Nat. Mater. 2 (2003) 320–323.
- [13] Y.H. Huang, R.I. Dass, Z.L. Xing, J.B. Goodenough, Science 312 (2006) 254–257.
- [14] J.M. Haag, B.D. Madsen, S.A. Barnett, K.R. Poeppelmeier, Electrochem. Solid State Lett. 11 (4) (2008) B51–B53.
- [15] Y.H. Huang, R.I. Dass, J.C. Denyszyn, J.B. Goodenough, J. Electrochem. Soc. 153 (7) (2006) A1266–A1272.
- [16] J.F. Moulder, W.F. Stickle, P.E. Sobol, K.D. Bomben, Handbook of X-ray Photoelectron Spectroscopy, Physical Electronics, Eden Prairie, MN, 1995.
- [17] National Institute of Standard and Technology (NIST), X-Ray Photoelectron Spectroscopy Database, <http://srdata.nist.gov/xps/>.
- [18] A.A. Guzelian, J.E.B. Katari, A.V. Kadavanich, U. Banin, K. Hamad, E. Juban, A.P. Alivisatos, R.H. Wolters, C.C. Arnold, J.R. Heath, J. Phys. Chem. 100 (1996) 7212–7219.
- [19] H. Falcon, J.A. Barbero, J.A. Alonso, M.J. Martínez-Lope, J.L.G. Fierro, Chem. Mater. 14 (2002) 2325–2333.
- [20] K. Tabata, S. Kohiki, J. Mater. Sci. Lett. 6 (1987) 1030.
- [21] R. Tan, Y. Zhu, Appl. Catal. B: Environ. 58 (2005) 61–68.
- [22] C. Thiriet, R.J.M. Konings, P. Javorský, N. Magnanib, F. Wastina, J. Chem. Thermodyn. 37 (2005) 131–139.
- [23] K. Popa, D. Sedmidubský, O. Beneš, C. Thiriet, R.J.M. Konings, J. Chem. Thermodyn. 38 (2006) 825–829.
- [24] Z. Cheng, S. Zha, M. Liu, J. Electrochem. Soc. 153 (7) (2006) A1302–A1309.
- [25] E. Povoden, M. Chen, A.N. Grundy, T. Ivas, L.J. Gauckler, J. Phase Equilib. Diff. 30 (2009) 12–27.
- [26] E. Povoden, A.N. Grundy, M. Chen, T. Ivas, L.J. Gauckler, J. Phase Equilib. Diff. 30 (2009) 351–366.
- [27] B.D. Madsen, W. Kobsiriphat, Y. Wang, L.D. Marks, S.A. Barnett, J. Power Sources 166 (1) (2007) 64–67.